Objective 2

Objective 2 Chapter 5

Optimization, and characterization study of the synthesized Zn metal-based nanomaterials

5.1. Introduction

Fabricating materials with the characteristic functionality demands optimization. The green synthesis process is optimized by fine-tuning numerous parameters to produce the desired nanoparticle properties, viz. size, shape, composition, and stability[1–4]. In this context, optimization entails screening a variety of plant extracts to determine which have the most effective phytochemical profiles for nanoparticle synthesis. Phytochemical quality and quantity can vary between plant species and even within the same plant. For example, leaves, stems, roots, and fruits may contain different bioactive chemicals. preliminary screening studies on various plant extracts are used to determine their efficacy in decreasing metal ions and stabilizing nanoparticles. These tests may include qualitative assays to determine the presence of certain phytochemicals with reducing characteristics, such as phenolics, flavonoids, alkaloids, and terpenoids[5–8]. Furthermore, quantitative examination of phytochemical content can reveal the relative abundance of these chemicals in various plant extracts. After screening for prospective candidate plant extracts, further optimization procedures include fine-tuning the synthesis settings to maximize nanoparticle yield, homogeneity, and stability. Which includes altering pH, temperature, reaction duration, and the plant extract-to-metal salt ratio[3,9–11]. Different pH can change the surface charge of nanoparticles, influencing colloidal stability, aggregation behaviour, and surface functionalization. The synthesis temperature influences the rate of chemical reactions and the kinetics of nanoparticle production. Optimization entails testing a variety of temperatures to determine the optimal temperature settings for effective nanoparticle synthesis while preserving control over particle size, size distribution, and shape[12,13]. The duration of the synthesis reaction influences the kinetics of nanoparticle production. Longer reaction periods may result in better nanoparticle yields because they provide more time for nucleation, growth, and stabilization processes, resulting in a greater conversion of precursor materials into nanoparticles. The rate at which nanoparticles are

stirred, as well as the presence of additional stabilizing agents (such as surfactants and polymers), can have an impact on their shape and dispersibility[14]. Stabilizing agents adsorb onto the nanoparticle surface, providing a barrier that prevents particle aggregation, Ostwald ripening, and sedimentation[15–17]. As important as optimization it also necessitates a thorough characterization of synthesized nanoparticles employing techniques such as Fourier Transform Infra-Red spectroscopy (FTIR), UV-Vis spectroscopy, X-ray diffraction (XRD), Dynamic Light Scattering (DLS), and Transmission Electron Microscopy (TEM)[18–21]. Scientists identify the crystalline phases present in nanoparticles by analyzing the diffraction patterns formed when X-rays contact their crystal lattice, estimate particle size using the Scherrer equation, and measure the degree of crystallinity. Individual nanoparticles can be directly visualized at high resolution using TEM, allowing researchers to identify their size, shape, and morphology with nanoscale precision[22,23]. HR-SEM and TEM images provide useful insights into nanoparticle homogeneity, dispersion, and aggregation, allowing for the optimization of synthesis parameters to attain the required properties[24,25]. FTIR spectroscopy is used to determine the chemical composition and functional groups on the surface of nanoparticles. FTIR spectra, that measure the absorption of infrared radiation by molecular vibrations in nanoparticle samples, offer information about surface coatings, capping agents, and interactions between nanoparticles and stabilizing ligands[24,26]. The yield % is a quality control metric that indicates the reproducibility and dependability of the synthesis process. Consistently high yields illustrate the synthesis method's durability and stability, ensuring the manufacture of nanoparticles with predictable properties[27–29].

This study was conducted to optimize reaction parameters to obtain stable Monometallic Bimetallic Quadrimetallic Nanomaterials (plant micronutrients such as Zinc, Copper, Iron, Manganese) which are made up with co-reduction procedure with the help of plant leaf extract as reducing and capping agents. Proper characterization of these materials was done to understand their unique properties which was later used for environmental applications.

Requisites:

- Glasswares
- Weighing Balance
- Flasks, reactors
- Magnetic Stirrer with Hot Plate
- Thermometer
- Centrifuge

- Sonicator
- UV-VIS spectrophotometer
- pH meter

5.2. Materials and Methods

5.2.1. Optimization study

The green synthesis of 3 types of metallic nanoparticles was subjected to optimization studies with UV–visible spectrophotometry conducted using a Thermo-Scientific Microplate Spectrophotometer, Multi-Skan sky (Serial number:1530-800894), to determine the Surface Plasmonic Resonance (SPR) of ZnO Monometallic nanoparticles (MNP), Zn-Cu Bimetallic Nanoparticles (BNP), Zn-Cu-Fe-Mn Quadrimetallic Nanoparticles (QMNP). Freshly prepared nanoparticle colloidal solutions were cooled to room temperature and UV scans were taken in a 96-well plate within the range of 200-800 nm. The baseline was stabilized using a blank. This allows for reliable measurement of changes in refractive index. The resulting SPR curves or UV-Vis spectra were analysed to extract essential information such as binding kinetics, affinity, concentration, and nanoparticle size and concentration[30,31]. Here, Temperature 80°C, Reaction Time 60 minutes, Stirring Speed 400 rpm, Concentration of PEG 5%, Final Volume 1000mL were kept constant, whereas the Concentration of aqueous leaf extract of *C. lutescens* and pH remained as variables. For MNP, only Zinc Oxide salt was used, for BNP 0.5M of both Zinc Oxide and Copper Sulphate was used and for QMNP Zinc Oxide, Copper Sulphate, Ferric Chloride, and Manganous sulphate were used. The nanoparticles underwent many rounds of washing with deionized water before being dried in a hot air oven overnight. Thus, the following equation (1) was used for deducing yield (%) in nanoparticles[32,33]

$$Yield\ (\%) = \frac{\text{Weight of the dried nanoparticles}}{\text{calculated weight of the salt}} \text{ x } 100 \text{ ----------eqn(1)}$$

5.2.2. Particle size analysis

DLS equipment performs particle size analysis by analyzing autocorrelation function of the scattered light and determining the particle size distribution. The study is based on variations in scattered light intensity induced by Brownian motion of particles. NanoPlus Common was used for measuring MNP, BNP, and QMNP hydrodynamic diameter by analyzing Brownian motion, and correlating it with an equivalent diameter for 14 days. The Zeta Sizer (Nano ZS90, Malvern Analytical) assesses colloidal dispersion stability, while Electrophoretic Light Scattering (ELS) measures particles' zeta potential and surface charge using Doppler shifts in scattered light[28].

5.2.3. Functional group analysis

For functional group analysis of MNP, BNP, and QMNP synthesized through aqueous leaf extract of *C.lutescens*, Fourier Transform Infra-Red Spectroscopy (FTIR) was done using Perkin Elmer Model: SPECTRUM 100 and FRONTIER IR on a colloidal nanoparticle solution. The solution was synthesized, centrifuged, resuspended, and lyophilized before recording spectra from 4000 cm^{-1} to 450 cm^{-1} with 2 cm resolution and five scans/samples using finely powdered nanoparticles and KBr[34].

5.2.4. Crystal structure determination

X-ray crystallography is one of the most often used techniques for determining crystal structure. This approach involves bombarding a crystal with X-rays, causing them to diffract in specific directions dependent on the arrangement of atoms within the crystal lattice. For X-ray diffraction (XRD) analysis, nanoparticle powdered samples were heated at 80°C to remove moisture and impurities. Analysis was conducted using a BRUKER AXS D8 FOC instrument with a Cu source at 1.5406 Å wavelengths in thin film mode. Crystalline structure and phase analysis were performed, and Scherrer's equation ($D=K\alpha/\beta\cos\Theta$) was utilized for size prediction, where D represents crystallite domain size, K is Scherrer's constant, α is wavelength, β is peak angular width, and Θ is diffraction angle[35,36].

5.2.5. Surface Morphology and Elemental Analysis

Surface Morphology is analyzed through Scanning Electron Microscopy (SEM) is a strong imaging method that examines surface morphology at high magnification. A concentrated electron beam examines the sample surface, producing secondary electrons, backscattered electrons, and other signals that are used to generate detailed pictures. SEM can disclose surface properties like roughness, texture, and topography at the nanoscale. Electron Dispersive Spectroscopy (EDS) is a technique used in conjunction with SEM or TEM to detect the unique X-rays generated by elements in a sample when blasted with electrons. EDS analyses the energy and intensity of these X-rays to offer quantitative and qualitative information about the surface's constituent composition. The JSM-7200F with Low Vacuum mode (LV) examined nanoparticle surface morphology from 10x to 1,000,000x magnification. Nanoparticle suspension underwent sonication to disperse aggregates, followed by air drying to remove solvent. Prepared substrates were mounted onto SEM stubs using double-sided carbon tape[37,38]. For Energy Dispersive X-ray (EDX) analysis, samples were dispersed in the solvent, air-dried on copper grids, and fixed with adhesive or conductive carbon tape to ensure stability[37].

5.2.6. Internal Morphology

For visualization of the internal morphology of a particle, Transmission Electron Microscopy (TEM) is preferred to be the gold standard. Sample preparation involved ultrasonication of the sample in aqueous solution, centrifugation, redispersion, and deposition onto a carbon-coated copper grid. The grid was then dried in a hot air oven at 60 °C for 4 hours before analysis using TECNAI G2 20 S-TWIN (200KV) TEM[39–41]. This TEM model is widely used for high-resolution imaging and investigation of nanoscale features, including the interior morphology of nanoparticles. The TEM's high-resolution imaging capabilities allow researchers to see the interior shape of nanoparticles on an atomic scale. It can disclose details about the nanoparticles' crystalline structure, lattice spacing, and flaws. The TEM can be used to study the interior microstructure of nanoparticles, such as grain boundaries, dislocations, and phase boundaries. It reveals information such as crystalline structure, lattice spacing, and flaws inside the nanoparticles.

5.2.7. Pore size and surface area measurement

Pore size and surface area determination is typically done with Brunner-Emmett-Teller (BET) surface area analysis (BET Autosorb iQ Station 1 Quantachrome Instruments, Austria) was used to estimate the specific surface area at a relative pressure range of 0.1-0.9[42,43]. Nitrogen gas (N_2) is employed as the adsorbate since it is both inert and easily available. Other gases, such as argon or carbon dioxide, can be utilized depending on the purpose. At low relative pressures (P/P_0), the adsorbed gases form a monolayer on the material's surface. Pore size distribution study is often carried out using Barrett-Joyner-Halenda (BJH) methodologies. Microporous materials have pores > 2 nm, mesoporous materials have pores ranging from 2-50 nm, and macroporous materials have pores <50 nm.

Before BET analysis, it is essential to degas the nanoparticle sample to remove adsorbed gases and contaminants and use a suitable dispersing agent or solvent, such as ethanol or isopropanol, to disperse the nanoparticles effectively. Prior Sonication of the nanoparticle suspension to break up agglomerates and promote uniform dispersion. Use a clean, pre-weighed sample container or crucible to contain the nanoparticles during analysis.

5.2.8. Decomposition behaviour

TGA analysis can reveal the temperature at which decomposition occurs, as well as the pace and extent of decomposition. Thermal degradation, volatile component desorption, phase shifts, and chemical reactions are all possible types of decomposition processes. The onset temperature of decomposition, or the temperature at which the decomposition process begins, can be calculated using TGA curves. The TGA curve usually exhibits a mass loss profile as a

function of temperature. Here, TGA studies were conducted in an inert atmosphere to evaluate the residual metal concentration in the plant extract samples with (TGA-50, Shimadzu). Monitoring of changes in mass, decomposition temperature, and reaction kinetics to characterize the thermal behaviour of the nanoparticles[44].

5.3. Results

5.3.1. Optimization study

Out of 30 permutations including Monometallic Nanoparticles (MNP), Bimetallic Nanoparticles (BNP), and Quadrimetallic Nanoparticles (QMNP), just one version from each parameter group was rigorously chosen for future rigorous evaluation and agricultural application. Specifically, the MNP configuration with 3% Aqueous Leaf Extract (ALE) at pH 9 emerged as the best choice (Table 5.1). Similarly, the BNP formulation with 3% ALE (pH 9) was found as the most promising (Table 5.2). Similarly, from the QMNP formulations, the composition containing 4% ALE (pH 9) was chosen for further exploration and agricultural application (Table 5.3).

Table 5.1. Optimization study of Monometallic Nanoparticles (MNP) with varying percentages of ALE and pH 5,7,9 w.r.t yield (%) of synthesized nanoparticles

Amount of Precursor salt	Precursor aqueous leaf extract (%) w/v	pH	Reaction Yield (g)	Reaction Yield (%)	UV-Spectra
40.69g ZnO	1%	5	16.23±0.15	39.90±0.36	Mid sharp slightly red shifted peak
	2%		16.63±0.12	40.87±0.23	Mid sharp slightly red shifted peak
	3%		17.40±0.10	42.77±0.25	Mid sharp slightly red shifted peak
	4%		17.93±0.06	44.07±0.12	Straight Sharp Peak
	5%		18.50±0.26	45.47±0.68	Broad slightly blue shifted Peak
	6%		18.50±0.26	45.47±0.68	Broad slightly blue shifted Peak
	7%		19.50±0.17	47.93±0.46	Broad slightly blue shifted Peak
	8%		19.80±0.10	48.67±0.25	Broad slightly blue shifted Peak
	9%		20.02±0.02	49.23±0.06	Broad slightly blue shifted Peak
	10%		20.24±0.22	49.73±0.58	Broad slightly blue shifted Peak
40.69g ZnO	1%	7	16.33±0.15	40.17±0.40	Mid sharp slightly red shifted peak
	2%		16.57±0.15	40.70±0.36	Mid sharp slightly red shifted peak
	3%		17.90±0.30	44.00±0.70	Straight Sharp Peak
	4%		18.60±0.17	45.73±0.40	Sharp noisy peak
	5%		18.83±0.25	46.27±0.60	Broad slightly blue shifted peak
	6%		19.63±0.25	48.27±0.60	Broad blue shifted peak
	7%		19.70±0.20	48.40±0.50	Broad blue shifted peak
	8%		20.31±0.20	49.93±0.50	Broad blue shifted peak
	9%		20.33±0.16	49.97±0.40	Saturated peak
	10%		20.72±0.17	50.93±0.45	Broad blue shifted peak
40.69g ZnO	1%	9	17.35±0.22	42.67±0.55	Sharp slight peak
	2%		18.82±0.13	46.27±0.31	Sharp slight peak
	3%		20.54±0.15	50.47±0.40	Straight Sharp peak
	4%		20.61±0.20	50.63±0.50	Broad blue shifted peak
	5%		20.59±0.16	50.60±0.44	Broad blue shifted peak
	6%		20.67±0.17	50.77±0.42	Broad blue shifted peak
	7%		20.55±0.22	50.50±0.53	Broad blue shifted peak
	8%		20.47±0.33	50.30±0.79	Broad blue shifted peak
	9%		21.34±0.41	52.47±1.03	Broad blue shifted peak
	10%		21.28±0.30	52.30±0.75	Broad blue shifted peak
LSD (p≤0.05)			**0.170**	**0.42**	

Note: Temperature: 80°C, Reaction Time: 60 minutes, Stirring Speed: 400 rpm, Concentration of PEG: 5%, Final Volume: 1000mL

Table 5.2. Optimization study of Bimetallic Nanoparticles (BNP) with varying percentages of ALE and pH 5,7,9 w.r.t yield (%) of synthesized nanoparticles

Amount of Precursor salt (0.5 molar)	**Precursor aqueous leaf extract (%) w/v**	**pH**	**Reaction Yield (g)**	**Reaction Yield (%)**	**UV-Spectra**
40.69g ZnO and 79.80g $CuSO_4$	1%	5	17.60±0.13	14.61±0.11	Mid sharp
	2%		17.47±0.22	14.50±0.18	Broad blue shifted peak
	3%		18.40±0.43	15.27±0.35	Straight Sharp peak
	4%		18.68±0.28	15.51±0.23	Mid sharp slightly red shifted peak
	5%		19.51±0.18	16.20±0.15	Mid sharp slightly red shifted peak
	6%		19.64±0.18	16.30±0.15	Noisy peak
	7%		20.13±0.10	16.70±0.09	Broad blue shifted peak
	8%		20.54±0.29	17.04±0.24	Broad Blue shifted peak
	9%		20.39±0.23	16.92±0.19	Broad blue shifted peak
	10%		20.84±0.14	17.29±0.12	Saturated peak
40.69g ZnO and 79.80g $CuSO_4$	1%	7	18.47±0.23	15.33±0.19	Slight noisy peak
	2%		18.57±0.40	15.41±0.33	Straight Sharp peak
	3%		18.70±0.23	15.52±0.19	Blue shifted noisy peak
	4%		18.70±0.19	15.52±0.16	Broad blue shifted peak
	5%		19.43±0.23	16.13±0.19	Broad peak
	6%		19.86±0.09	16.48±0.07	Broad peak
	7%		19.68±0.12	16.34±0.10	Broad peak
	8%		20.39±0.25	16.92±0.21	Broad blue shifted peak
	9%		20.25±0.27	16.81±0.23	Broad blue shifted peak
	10%		20.46±0.32	16.98±0.26	Saturated peak
40.69g ZnO and 79.80g $CuSO_4$	1%	9	17.86±0.24	14.83±0.20	Mid sharp red shifted peak
	2%		17.55±0.47	14.57±0.39	Straight Sharp peak
	3%		18.37±0.30	15.25±0.24	Noisy peak
	4%		18.39±0.33	15.26±0.28	Blue shifted broad peak
	5%		19.60±0.33	16.27±0.28	Blue shifted broad peak
	6%		19.61±0.38	16.28±0.31	Broad blue shifted peak
	7%		20.76±0.21	17.23±0.17	Blue shifted broad peak
	8%		20.49±0.34	17.01±0.28	Broad peak
	9%		21.35±0.36	17.72±0.30	Broad peak
	10%		21.53±0.22	17.87±0.19	Saturated peak
LSD (p≤0.05)			**0.222**	**0.18**	

Note: Temperature: 80°C, Reaction Time: 60 minutes, Stirring Speed: 400 rpm, Concentration of PEG: 5%, Final Volume: 1000mL

Table 5.3. Optimization study of Quadrimetallic Nanoparticles (BNP) with varying percentages of ALE and pH 5,7,9 w.r.t yield (%) of synthesized nanoparticles.

Amount of Precursor salt	**Concentration of Precursor aqueous leaf extract (%) w/v**	**pH**	**Reaction Yield (g)**	**Reaction Yield (%)**	**UV-Spectra**
40.69g ZnO, 79.80g $CuSO_4$, 81.10g $FeCl_3$, 84.51g $MnSO_4•H_2O$	1%	5	15.48±0.21	5.41±0.07	Slight sharp peak
	2%		15.59±0.23	5.45±0.08	Slight noisy peak
	3%		16.62±0.16	5.81±0.06	Sharp peak
	4%		16.47±0.39	5.76±0.14	Sharp peak
	5%		16.48±0.45	5.76±0.16	Sharp peak
	6%		18.42±0.23	6.44±0.09	Broad peak
	7%		18.67±0.29	6.53±0.10	Broad peak
	8%		18.47±0.14	6.46±0.05	Broad peak
	9%		18.51±0.40	6.47±0.14	Broad peak
	10%		18.63±0.50	6.51±0.18	Broad peak
40.69g ZnO, 79.80g $CuSO_4$, 81.10g $FeCl_3$, 84.51g $MnSO_4•H_2O$	1%	7	19.34±0.27	6.76±0.10	Mid sharp peak
	2%		19.66±0.18	6.87±0.06	Mid sharp peak
	3%		19.45±0.33	6.79±0.12	Broad peak
	4%		20.43±0.13	7.14±0.05	Mid sharp peak
	5%		20.68±0.22	7.23±0.08	Broad peak
	6%		21.66±0.23	7.57±0.08	Broad peak
	7%		22.61±0.16	7.90±0.06	Straight Sharp peak
	8%		22.22±0.20	7.77±0.07	Broad peak
	9%		22.45±0.29	7.85±0.10	Broad peak
	10%		23.49±0.13	8.21±0.04	Broad peak
40.69g ZnO, 79.80g $CuSO_4$, 81.10g $FeCl_3$, 84.51g $MnSO_4•H_2O$	1%	9	21.61±0.25	7.55±0.09	Sharp peak
	2%		22.21±0.29	7.76±0.10	Broad blue shifted peak
	3%		22.18±0.18	7.75±0.07	Broad blue shifted peak
	4%		23.33±0.21	8.15±0.07	Sharp peak
	5%		23.51±0.22	8.22±0.07	Broad blue shifted peak
	6%		24.25±0.14	8.47±0.05	Broad blue shifted peak
	7%		23.47±0.27	8.20±0.10	Sharp peak
	8%		24.44±0.29	8.54±0.10	Broad blue shifted peak
	9%		23.91±1.21	8.36±0.42	Broad blue shifted peak
	10%		23.39±0.25	8.18±0.09	Broad blue shifted peak
LSD (p≤0.05)			**0.279**	**0.10**	

Note: Temperature: 80°C, Reaction Time: 60 minutes, Stirring Speed: 400 rpm, Concentration of PEG: 5%, Final Volume: 1000mL

5.3.2. Surface Plasmon Resonance

The colloidal NP formation was validated through UV-visible absorption spectroscopy at a 200-800 nm wavelength range. Surface plasmon resonance (SPR) of the nanoparticles' excitation peak was recorded at lower MNP wavelengths, creating a blue shift, as shown in the UV-visible spectra (Fig.5.1). The SPR peaks were reasonably sharp and narrow at ALE 1-4% at all pH. However, the SPR peaks broadened with increased ALE proportions beyond 5% across the nanomaterial types i.e., MNP, BNP and QMNP (Fig. 5.1, 5.2, 5.3). In the batch experiments, the synthesis of MNP, BNP and QMNP was optimized with 1-10%. ALE (w/v) and at a pH range of 5 to 9 to reproduce the uniform size and shapes of the NPs and confirm the maximum yield (%). Throughout the batch experiments, the size of the nanomaterials was consistently within the range of 200 to 400 nm at pH 5, 7, and 9, and a sharp peak was recorded with 3% ALE for both MNP and BNP and 4% for QMNP. The batch experiments confirmed that alkaline conditions (pH 9) are most suitable for forming uniform NP crystals[45]. At higher pH 9 tended to acquire substantial negative surface charge; the size of the NPs is confirmed by the peak near 400 nm (Table 5.1, 5.2, 5.3). The optimized synthetic conditions (i.e., 3% ALE at pH 9 for MNP and BNP) were confirmed after repeating the process three times, which also assured stable yield (%). Hence, it can be postulated that the phytoconstituent-rich ALE of *C. lutescens* acted as an efficient reducing and surface-stabilizing agent in forming MNP and BNP. Additionally, the engineered NPs were stable at room temperature at intervals of days 7, 14, and 25 days (Fig. 5.4, 5.6); our results are consistent with previous findings[20,21].

5.3.3. Reaction Yield (%)

The reaction yield (%) were derived from equation-------(1). For MNP the average nanoparticle yield (%) was observed in pH 9 at 3% ALE (50.47±0.40) followed by pH 7 at 3% ALE (44.00±0.70) (Table 5.1.) conversely, in the case of BNP, the mean yield (%) was observed in 2% ALE at pH 7 (15.41±0.33) followed by 2% ALE at pH9 (14.57±0.39) (Table 5.2). Meanwhile, QMNP showed average yield (%) at 7% ALE at pH7 (7.90±0.06) followed by 4% ALE at pH 9 (8.15±0.07) (Table 5.3.). Based on yield (%) and a sharp SPR peak, characterization was narrowed down further. Out of 30 combinations of MNP, BNP and QMNP only 1 from each optimized parameter was selected for further characterization and application in agriculture. From MNP, 3% ALE (pH 9) was selected, similarly for BNP, 2% ALE (pH 9) was selected and from QMNP 4% ALE (pH 9) was taken for further studies.

5.3.4. Particle size analysis

Particle size analysis is done with a DLS instrument. A low polydispersity index (PDI) indicates particle homogeneity, which may boost the biological applications of nanoparticles[46]. The PDI of the biosynthesized MNP was 0.312 and that of BNP was 0.554, indicating that the particles were mono-dispersed in nature (Table 5.4.). A low polydispersity index (PDI) indicates particle homogeneity, which may boost nanoparticles' biological applications. The PDI of the biosynthesized QMNP was documented to be 1.14 indicating that the particles were highly Poly-dispersed with multiple particle size populations (Table 5.5). The Zeta analyser helps us to understand the Zeta potential of MNP and BNP was observed to be - 11.3 mV and -17.4 mV respectively whereas the Zeta potential of QMNP was delineated to be -16 Mv (Table 5.4, 5.5). DLS study confirmed the stability of the synthesized MNP and BNP was observed for 14 days with the average hydrodynamic diameter decreasing with increasing pH (Fig. 5.5). The stability of the synthesized QMNP was observed for 14 days and the same trend was observed (Fig.5.6.); meanwhile stability of the synthesized MNP, BNP and QMNP at room temperature was observed at an interval of day 7, 14, 25 using UV-Vis Spectra (Fig. 5.4, 5.6). MNP, BNP stable peaks were observed at pH 7, 9 (Fig. 5.4); moreover, stable peaks observed at pH 4 in case of QMNP (Fig. 5.6)

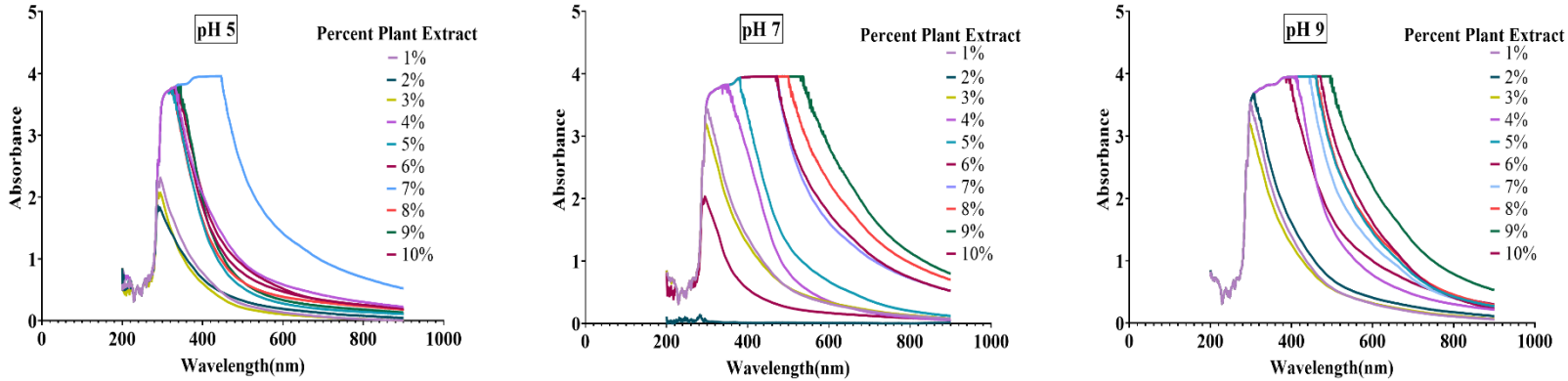

Fig. 5.1. Optimization study of Monometallic Nanoparticles (MNP) with Aqueous Leaf Extract (ALE) 1-10% with pH5,7,9.

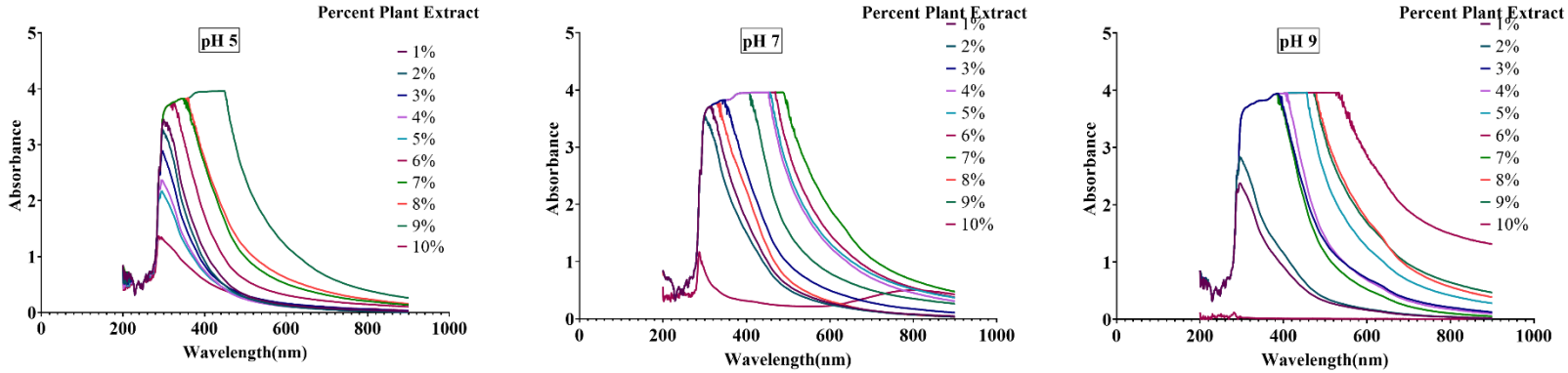

Fig.5.2. Optimization study of Bimetallic Nanoparticles (BNP) with Aqueous Leaf Extract (ALE) 1-10% with pH5,7,9.

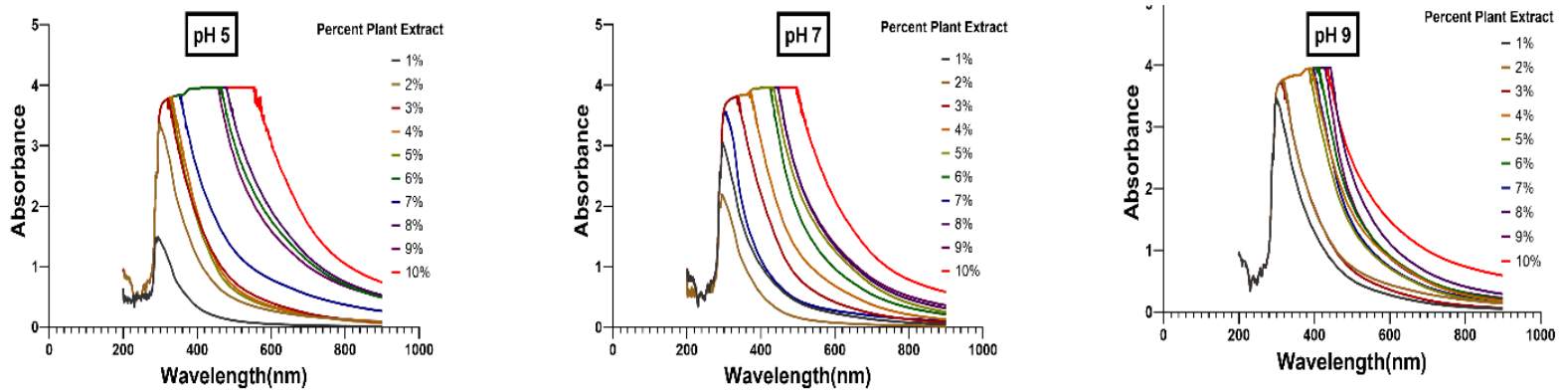

Fig.5.3. Optimization study of Quadrimetallic Nanoparticles (QMNP) with Aqueous Leaf Extract (ALE) 1-10% with pH 5, 7, 9.

Table 5.4. Average Hydrodynamic Diameter, Zeta Potential, and BET Surface area of MNP and BNP Nanomaterials (Mean ± SD)

Material	Zeta Potential (mV)	Average Hydrodynamic Diameter (nm)	Poly Dispersity Index (PDI)	Surface area (m^2/g)	Pore Volume (cc/g)	Pore radius Dv(r) Å
MNP	-11.3	100	0.312	7.012	0.019	21.61
BNP	-17.4	100	0.554	17.122	0.020	21.619

Table 5.5. Average Hydrodynamic Diameter, Zeta Potential, and BET Surface area of Quadri metallic Nanoparticles (QMNP) (Mean ± SD)

Material	Zeta Potential (mV)	Average Hydrodynamic Diameter(nm)	Polydispersity Index (PDI)	Surface area (m^2/g)	Pore Volume (cc/g)	Pore radius Dv(r) Å
QM-NP	-16 ± 1.0	99.6 ± 10.5	1.14 ± 0.311	3.662	0.010	19.066

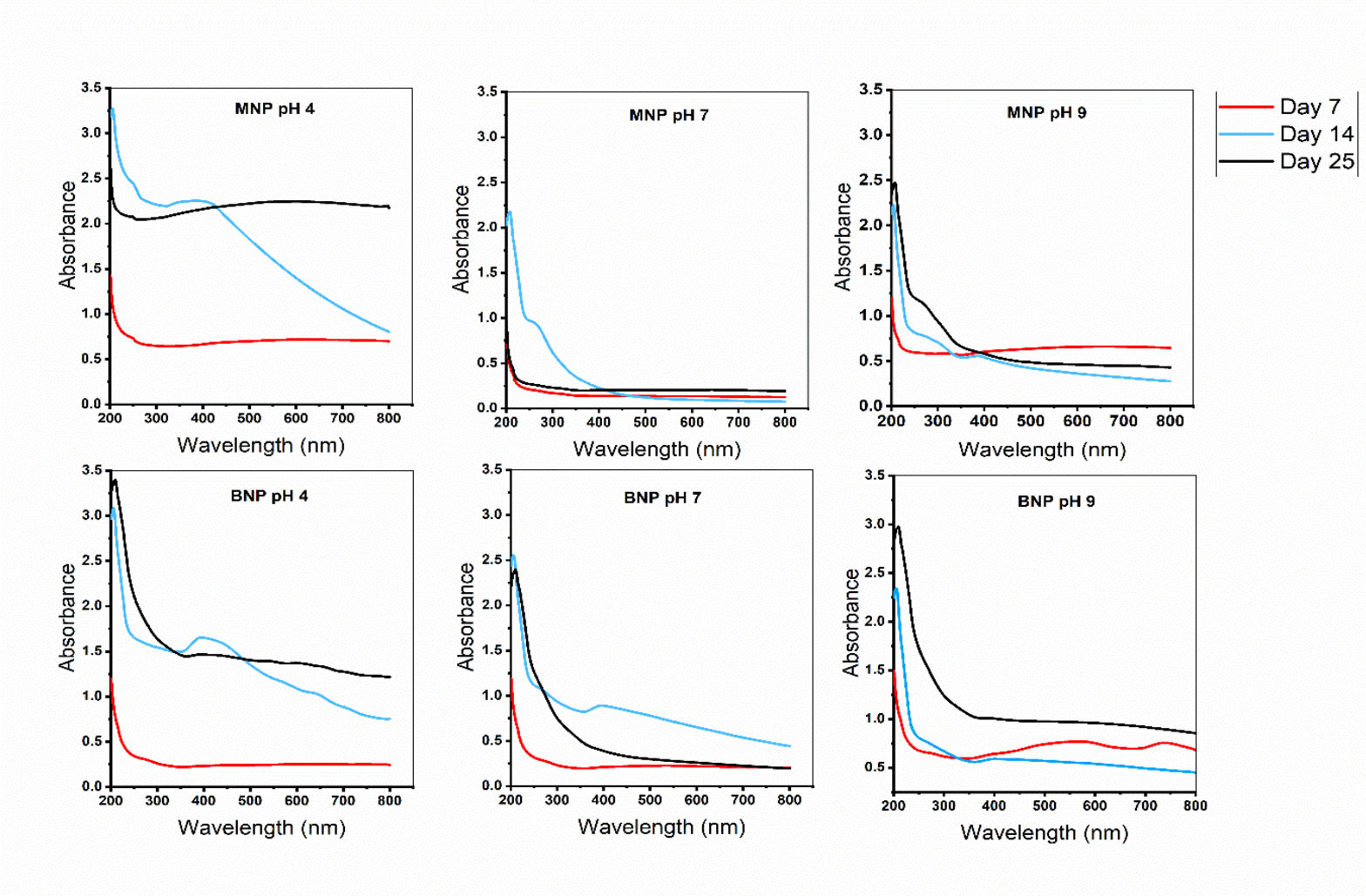

Fig. 5.4. Stability cross checking of MNP and BNP at room temperature at an interval of day 7, 14, 25 for the synthesized nanomaterials using UV-Vis Spectra.

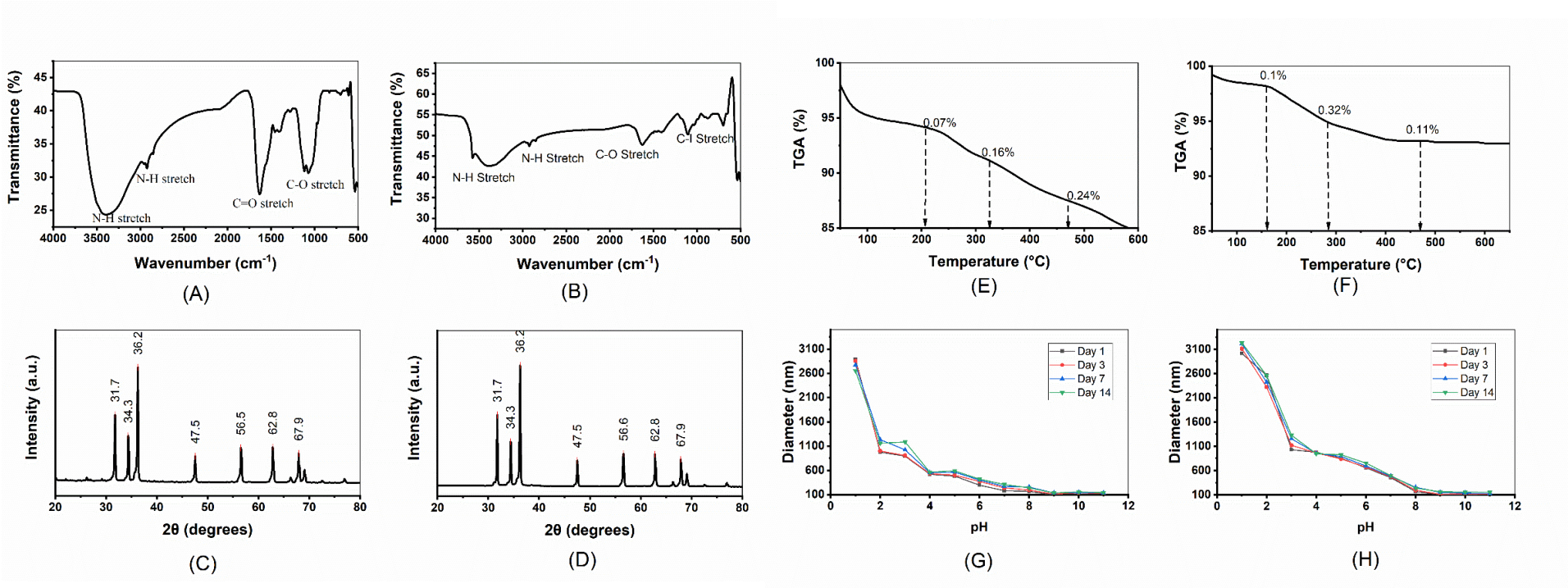

Fig. 5.5. FTIR Spectra of green synthesized MNP (A) and BNP (B) showing various functional groups of plant phytoconstituents bound to the surface of the material. Powdered X-Ray Diffraction (P-XRD), study of green synthesized MNP (C) and BNP (D) showing crystallinity peaks, Thermo-Gravimetric Analysis (TGA) plot showing the (%) loss of weight of MNP (E) and BNP (F) at Temperature above 500ºC. Degrees of change in Hydrodynamic diameter with various pH range from 4-9 w.r.t to particle diameter (nm) over a period of Day 1-14 for MNP (G), BNP(H).

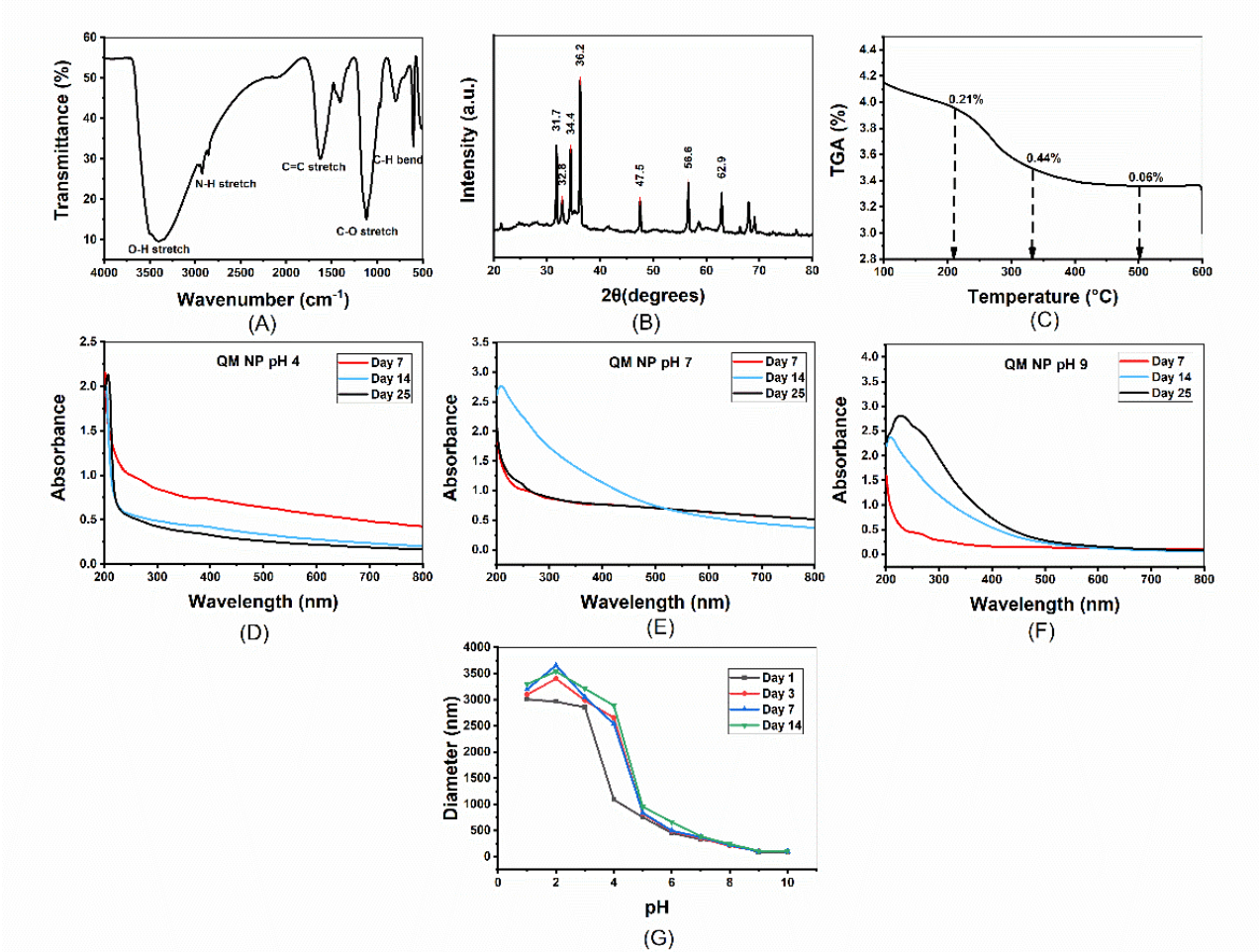

Fig. 5.6. FTIR Spectra (A) of green synthesized QMNP showing various functional groups of plant phytoconstituents bound to the surface of material. Powdered X-Ray Diffraction (P-XRD) study of green synthesized QMNP (B) showing crystallinity peaks. Thermo Gravimetric Analysis (TGA) plot showing the (%) loss of weight of QMNP (C) at Temperature above 500ºC. Stability of synthesized QMNP (D-F) at room temperature with various pH range from 4-9 at an interval of day 7,14,25 using UV-Vis Spectra and Degrees of change in Hydrodynamic diameter with various pH range from 4-9 w.r.t to particle diameter (nm) QMNP (G) over a period of 1-14 days in DLS study respectively.

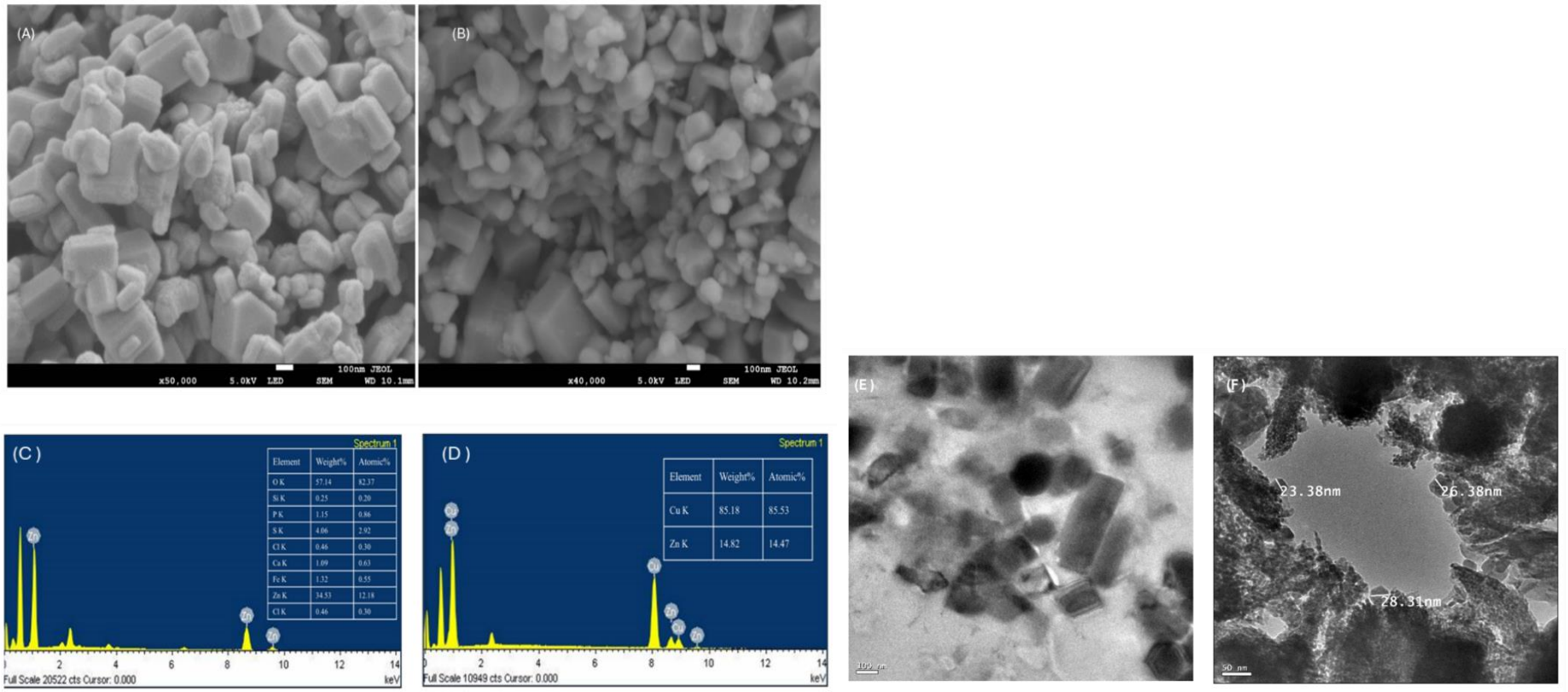

Fig. 5.7. Field Emission Scanning Electron Microscope (FE-SEM) micrographs and Transmission Electron Microscope (TEM) micrographs showing green synthesized MNPs (A, C, E) and BNP (B, D, F) in the scale of 100nm i.e., 50,000X. Energy Dispersive X-ray (EDX).

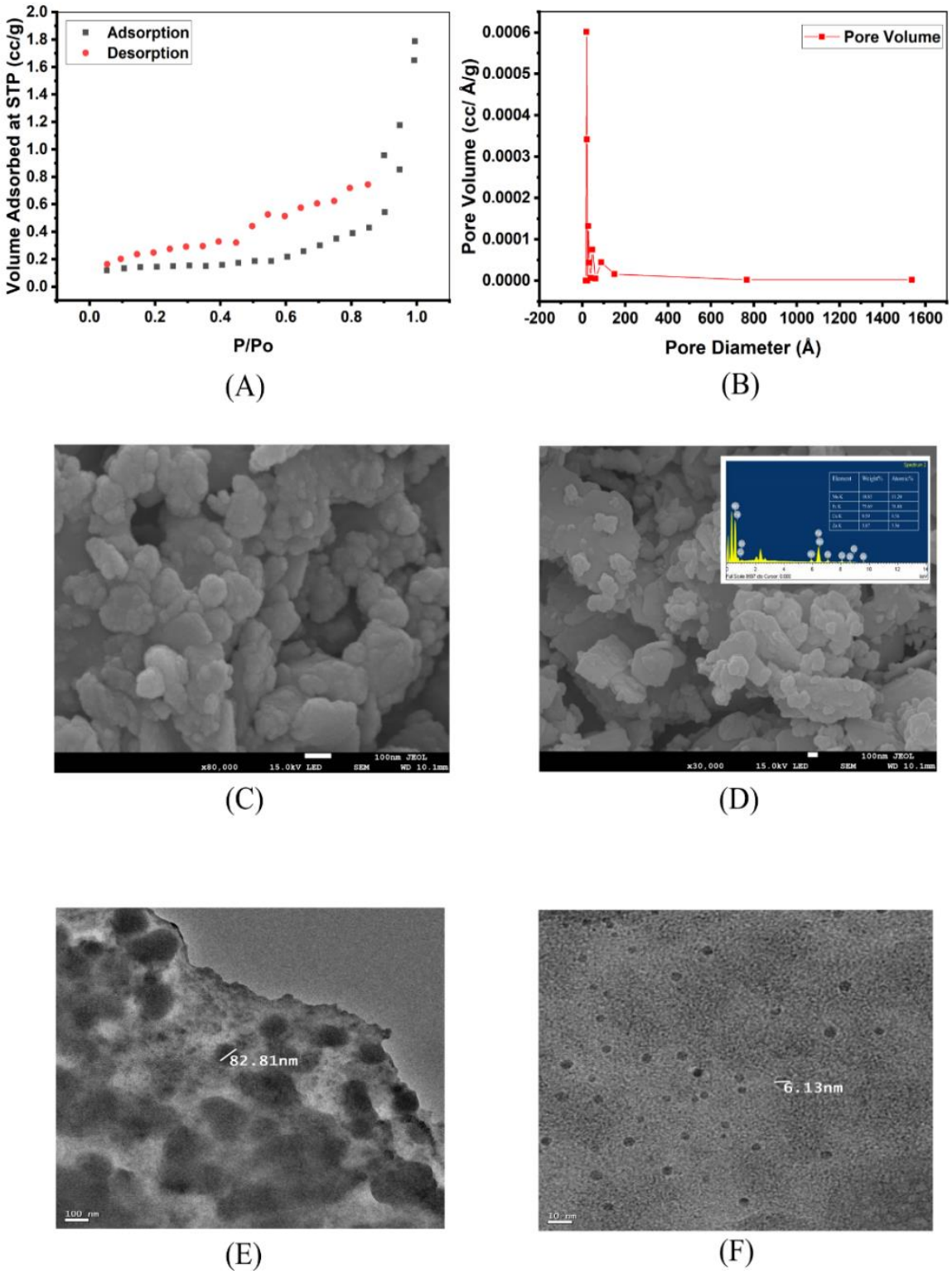

Fig. 5.8. BET-BJH plot of QMNP (A, B). Field Emission Scanning Electron Microscope (FE-SEM) (C, D) of QMNP along with embedded Energy Dispersive X-ray (EDX) micrographs (D) Transmission Electron Microscope (TEM) micrographs showing green synthesized QMNP (E, F) in the scale of 100 nm i.e., 50,000X.

5.3.5. Functional group analysis

The potential functional groups that promoted synthesis of MNP and BNP were investigated through FTIR (Fig. 5.5.). The characteristic bands of both the Nanoparticles are observed at 3490 cm^{-1}, 1565 cm^{-1}, 1124 cm^{-1} showed and 689 cm^{-1}. The potential functional groups that promoted synthesis of QMNP were investigated through FTIR (Fig. 5.6.). The characteristic bands of both the Nanoparticles are observed at 3500 cm^{-1}, 2990 cm^{-1},1600 cm^{-1}, 1565 cm^{-1}, 595 cm^{-1}

5.3.6. Crystal structure determination

The diffraction peaks for MNP were recorded at 2θ values of 31.75°, 34.34°, 36.24°, 47.52°, 56.56°, 62.79° and 69.08° conforming to the crystal phases [100], [002], [101], [102], [110], [103] and [112] planes; approximately the same 2θ values of 31.74°, 34.39°, 36.23°, 47.52°, 56.57°, 62.84° and 67.93° were recorded for the crystal phases for MNP and BNP (Fig.5.5.). The XRD diffraction peaks for QMNP were recorded at 2θ values of 31.78°, 32.36°, 34.44°, 36.26°, 47.55°, 56.61°, and 62.87° conforming to the crystal phases [100], [002], [101], [102], [110], [103] and [112] planes. The average crystallite size was recorded to be 49.69nm and average d spacing was calculated to be 0.1246 (Fig. 5.6.)

5.3.7. Surface Morphology and Elemental Analysis

The MNP nanocrystals with a diameter of 30-85 nm are illustrated in the FE-SEM micrographs (Fig. 5.7.). The FE-SEM micrographs also show the uniform arrangement of NPs into tightly packed structures. EDX detailed and confirmed the elemental makeup vis-à-vis the higher percentage of Zn in the MNP and Cu-Zn in the BNP (Fig.5.7.). The Quadrimetallic nanoparticle size was in a range of 20–50 nm connected to form clusters (Fig.5.8.)

5.3.8. Internal Morphology

TEM micrographs show that both the MNP and BNP have majorly rectangular and spherical shapes (Fig. 5.7), less consistent crystalline forms are seen as MNP. In the case of QMNP, TEM micrographs show that multilayered particles have formed as multiple metals were subjected to co-reduction at high temperatures and pH 9 (Fig. 5.8).

5.3.8.1. Pore size and surface area measurement

Brunner-Emmett-Teller (BET) analysis showed that the surface area was 7.012 m2 g^{-1}, with a pore volume of 0.019 cubic centimetres g^{-1} and a pore radius Dv(r) of 21. 615Å, for MNP and 17.122 m^2 g^{-1} and pore radius Dv(r) of 21.619 Å for BNP (Table 5.4.). Type IV isotherm curves were visible in the N2 adsorption-desorption isotherms manifested the surface area,

total pore volume, and pore size distribution of nanoparticles of the MNP and BNP. The particle sizes are homogeneous and aligned with their textural properties. BET surface area for QMNP was calculated by BJH Plot and was found to be 3.662 m^2/g with a pore volume of 0.010 cc/g and a pore radius Dv(r) of 19.066 Å (Table 5.5. Fig. 5.8). Type IV isotherm curves were visible in the N2 adsorption-desorption isotherms manifested in the surface area, total pore volume, and pore size distribution of the biosynthesized nanoparticles.

5.3.9. Decomposition behaviour

The TGA profile revealed a steady weight loss with three nearly sharp shifts at 100 °C, 230 °C, 330 °C, and 480 °C, followed by a virtually constant plateau for MNP, similarly, for BNP it was 100 °C, 160 °C, 290 °C, 480 °C (Fig. 5.5). Thus, it appears that annealing at temperatures above 400 °C will always result in the formation of stable Zn-based nanoparticles. The TGA profile revealed a steady weight loss with three nearly sharp shifts at 230 °C, 330 °C, and 500 °C, followed by a virtually constant plateau for QMNP (Fig. 5.6).

5.4. Discussion

The observed trends in the Surface Plasmon Resonance (SPR) peaks for Monometallic Nanoparticles (MNP), Bimetallic Nanoparticles (BNP), and Quadrimetallic Nanoparticles (QMNP) with different concentrations of Aqueous Leaf Extract (ALE) and pH levels provide valuable insights into the nanoparticle synthesis process and the role of these parameters in controlling nanoparticle properties. To begin, the sharper and narrower SPR peaks obtained at lower ALE concentrations (1-6%) and specific pH values (pH 5, 7, and 9 for BNP; while for QMNP it is pH 9, 7, 5 at 4% and 1% ALE indicate a more regulated and uniform nanoparticle production process under these conditions[21,47–49]. This behaviour can be related to slower nucleation and growth kinetics at lower ALE concentrations and certain pH values, which result in nanoparticles with more uniform size and shape distributions. Broader SPR peaks at higher ALE concentrations (7-10%) for MNP and under specific ALE concentrations aggregation or non-uniform particle size distributions was observed. At greater ALE concentrations, nanoparticle nucleation and growth may occur more quickly, resulting in enhanced nanoparticle aggregation or polydispersity, and hence larger SPR peaks[21,47]. Similarly, changes from ideal pH conditions might affect nucleation and growth kinetics, resulting in non-uniform nanoparticle production. The validation of colloidal nanoparticle creation using UV-visible absorption spectroscopy confirms the observed trends in SPR peaks, giving additional evidence for effective nanoparticle synthesis under optimal conditions. The steady preservation

of pH between 5 and 9 with 1 M NaOH and 1 N HCl ensures reproducibility and control over the synthesis process, further confirming the optimization method.

The reaction yield has a direct impact on the scalability of nanoparticle synthesis. High yields are required for scaling up production to satisfy commercial or industrial demands efficiently. Scalability refers to moving from laboratory-scale synthesis to higher production scales while retaining consistent product quality, efficiency, and cost-effectiveness. Achieving high yield at the laboratory scale is essential for successful scale-up because it lays the groundwork for optimizing reaction conditions and process parameters for higher volumes. Scalability criteria include reactor design, mixing efficiency, heat and mass transmission, safety standards, and environmental impact. High reaction yields help to optimize resource utilization by maximizing the conversion of precursor materials into desirable nanoparticles. Efficient resource utilization is crucial for reducing production costs and minimizing the environmental impact of nanoparticle synthesis[47,50]. Optimizing reaction parameters, such as precursor concentrations, reaction duration, temperature, and catalyst utilization, can improve resource efficiency while reducing waste formation. By increasing yield, fewer resources are lost on unreacted precursors, byproducts, or contaminants, resulting in more sustainable and cost-effective nanoparticle production processes[51]. Maximizing reaction yield is critical for reducing waste generated during nanoparticle manufacturing. High yields lower the number of unwanted precursors, side products, and by-products, resulting in less waste per unit of product manufactured. Waste reduction not only minimizes environmental effects but also lowers disposal costs and increases overall process efficiency. Waste minimization strategies include optimizing reaction conditions, using effective purification and separation procedures, recycling solvents and catalysts whenever possible, and building closed-loop processes to reduce emissions and waste streams.

The biosynthesized nanoparticles were negatively charged in water, which also infers nanoparticle surface charge and colloidal stability. The polydispersity index (PDI) is a critical indication of nanoparticle homogeneity, with important implications for their prospective applications. Biosynthesized Monometallic Nanoparticles (MNP) and Bimetallic Nanoparticles (BNP) have relatively low PDIs of 0.312 and 0.554, indicating a high degree of monodispersity[52,53]. This homogeneity in particle size distribution is beneficial to biological applications because it assures constant behaviour and interactions within biological systems. The low PDI values indicate that the produced nanoparticles have minimal particle size variation, which is advantageous for achieving reproducible results and maximizing their

effectiveness of biomedical applications involving drug delivery and imaging. Conversely, the substantially higher PDI of 1.14 reported for Quadrimetallic Nanoparticles (QMNP) indicates a higher degree of polydispersity, as seen by numerous particle-size [54–56]. This greater diversity of particle sizes could be caused by changes in synthesis conditions or the presence of various metal components, resulting in heterogeneous nanoparticle production. While polydispersity may limit some applications that need exact control over particle size, such as targeted medication delivery, it may be beneficial in others, such as catalysis, where a variety of particle sizes can improve activity and selectivity. The zeta potential measurement provides information on the surface charge and colloidal stability of biosynthesized nanoparticles. The negatively charged zeta potentials of MNP (-11.3 mV) and BNP (-17.4 mV) in water indicate the presence of surface-bound functional groups or ions that aid in stabilizing nanoparticles through electrostatic repulsion[52,53]. This electrostatic stabilization prevents particle aggregation while also preserving colloidal stability, which is essential for maintaining nanoparticle properties and behaviour in biological and environmental settings. For MNP and BNP, the DLS data show that the nanoparticles remained stable for 14 days, with the average hydrodynamic diameter decreasing as the pH increased. This observation shows that higher pH conditions help to improve nanoparticle stability, presumably by boosting electrostatic repulsion and reducing aggregation or sedimentation. The decrease in hydrodynamic diameter with rising pH suggests a more diffused and homogenous dispersion of nanoparticles in solution, implying greater colloidal stability. A similar trend was observed in QMNP[57,58]. Furthermore, stability evaluations using UV-Vis spectra show the long-term stability of MNP, BNP, and QMNP at room temperature, with stable peaks found at specified pH values over different intervals (days 7, 14, and 25). MNP and BNP exhibited stable peaks at pH 7 and 9, indicating excellent stability in slightly acidic to neutral environments. In contrast, persistent peaks for QMNP were detected at pH 4, indicating that lower pH settings may be preferable for preserving colloidal stability. These pH-dependent stability patterns are similar with the DLS findings, emphasising the relevance of pH management in influencing nanoparticle stability and behaviour in solution[18,57,58].

MNP and BNP exhibit distinctive bands at 3490 cm^{-1}, indicating stretching vibrations of -NH or amine groups found in proteins, amino acids, or other biomolecules in aqueous leaf extract utilized for nanoparticle synthesis[59–61]. The detected band at 1565 cm^{-1} is because of the stretching vibrations of C=O bonds, indicative of carbonyl groups presents in proteins and aldehydes. The 1124 cm^{-1} band corresponds to C-O stretching vibrations, which are often

associated with hydroxyl or carboxylic acid groups found in biological compounds[62–64]. The band at 689 cm^{-1} implies stretching vibrations of C-I bonds, possibly due to iodine-containing chemicals in the leaf extract. The FTIR spectra of QMNP show distinct bands at 3500 cm^{-1}, indicating stretching vibrations of OH or alcohol groups. These vibrations could be caused by sugars, polyphenols, or other hydroxyl-containing biomolecules found in the leaf extract. The band at 2990 cm^{-1} resembles to -NH stretching vibrations, suggesting the presence of amine groups in proteins or amino acids. The band at 1600 cm^{-1} indicates stretching vibrations of alkene or benzene groups, which can be found in aromatic compounds or unsaturated fatty acids. The bands at 1565 cm^{-1} correspond to C-O stretching vibrations, like MNP and BNP, whereas the band at 595 cm^{-1} suggests stretching vibrations of C-H bonds seen in hydrocarbons[65–68].

The crystal planes [100], [002], [101], [102], [110], [103], and [112] correspond to the diffraction peaks at certain 2θ values for MNPs (31.75°, 34.34°, 36.24°, 47.52°, 56.56°, 62.79°, and 69.08°) and BNPs (31.74°, 34.39°, 36.23°, 47.52°, 56.57°, 62.84°, and 67.93°). These diffraction patterns are characteristic of the hexagonal Wurtzite crystal structure, which is commonly found in zinc-based nanoparticles[69–71]. The diffraction peaks and 2θ values of MNPs and BNPs are identical, indicating that the crystal structure is preserved despite the addition of metal species to the bimetallic nanoparticles. This retention of crystal structure suggests the creation of solid solution or alloy nanoparticles with Face-Centered Cubic (FCC) geometry, in which the lattice constants and crystal symmetry are essentially preserved[72–74]. In QMNPs, diffraction peaks at 2θ values of 31.78°, 32.36°, 34.44°, 36.26°, 47.55°, 56.61°, and 62.87° correspond to crystal planes [100], [002], [101], [102], [110], [103], and [112], respectively. These diffraction sequences are compatible with the quasi spherical[75–78]. The existence of diffraction peaks at similar 2θ values across all three nanoparticle types confirms the fabrication of crystalline nanoparticles with specified crystallographic planes. Furthermore, calculating the average crystallite size and d spacing yields quantitative data on the size and spacing of crystalline domains inside nanoparticles.

Field-Emission Scanning Electron Microscopy (FE-SEM) micrographs that reveal important information on the size distribution, shape, and arrangement of Monometallic Nanoparticles (MNPs) and Bimetallic Nanoparticles (BNPs). The detected nanocrystals have dimensions extending from 30-85 nm, with prominent hexagonal Wurtzite and Zinc blende structures, which are typical of zinc-based nanoparticles[78–80]. The occurrence of both hexagonal Wurtzite and Zinc blende structures in nanoparticles suggests the coexistence of distinct crystal phases,

which can be caused by changes in synthesis circumstances or the presence of impurities. The observed shape-size dynamics of MNPs and BNPs, notably the creation of nanocrystals smaller than 100 nm, can be linked to the temperature range of 60–80 °C throughout the biosynthesis process. Within this temperature range, nucleation and growth kinetics are optimized, resulting in smaller nanocrystals with well-defined morphologies. The uniform arrangement of nanoparticles into densely packed formations shown in the FE-SEM micrographs supports the creation of ordered assemblies or aggregates, which could be caused by interactions amongst nanoparticles via the van der waals forces or electrostatic interactions nanoparticles[78–80]. The Energy-Dispersive X-ray spectroscopy (EDX) study offers detailed information about the nanoparticles' elemental makeup. The larger percentage of zinc in MNP and copper-zinc in BNP, as validated by EDX, supports the synthesized nanoparticles' bimetallic origin and elemental composition. Other elements, such as oxygen, carbon, and trace metals, may be impurities or residues from the production process. The Quadrimetallic Nanoparticles (QMNPs) have a size range of 20 to 50 nm and cluster together, as shown in the FE-SEM micrographs. Cluster formation could be caused by the agglomeration of various nanoparticles during synthesis or sample preparation[81]. The reported cylindrical and quasi-spherical morphologies of QMNPs are consistent with prior results, indicating that synthesis factors may influence nanoparticle morphology.

MNPs and BNPs internal morphology is done with Transmission Electron Microscope (TEM) micrographs which show mostly rectangular and spherical forms at higher pH 9. Variations in synthesis parameters, such as precursor concentrations, reaction rates, and nucleation processes, could account for the observed morphologies[82–84]. Rectangular forms are commonly associated with anisotropic growth, which occurs preferentially along specific anisotropic orientations, resulting in elongated nanoparticles. Spherical shapes, on the other hand, imply isotropic development, in which crystals grow equally in all directions, producing symmetrically formed nanoparticles. The presence of flaws, grain boundaries, or impurities within MNPs may explain the less uniform crystalline forms observed, which can alter crystallinity and morphology. In contrast, TEM micrographs of QMNPs show multilayered particles, showing the inclusion of different metals during co-reduction at high temperatures and neutral pH 7. The multilayered structure shows that metal atoms are deposited or nucleated sequentially, resulting in the creation of separate layers or shells within nanoparticles. The neutral pH environment pH 7 may assist in the co-reduction of several metal ions by increasing the creation of stabilizing intermediates used in nanoparticle synthesis[85,86]. Furthermore, the

high temperature may increase metal atom mobility, allowing them to diffuse and incorporate into the developing QMNPs more readily.

The Brunauer-Emmett-Teller (BET) study of monometallic nanoparticles (MNPs) and bimetallic nanoparticles (BNPs) gives useful information about their textural features, viz. pore volume, surface area, and pore size distribution. MNPs have a surface area of 7.012 m^2/g, pore volume of 0.019 cc/g, and pore radius (Dv(r)) of 21.615 Å. Similarly, BNPs had a surface area of 17.122 m^2/g and a pore radius of 21.619 Å. The Type IV isotherm curves in the N_2 adsorption-desorption isotherms indicate mesoporous materials, which have pores with sizes ranging from 2-50 nm[87–89]. The BET surface area of Quadrimetallic Nanoparticles (QMNPs) was determined using the BJH Plot method and found to be 3.662 $m^2\ g^{-1}$. The pore volume was 0.010 cubic centimetre g^{-1} and the pore radius was 19.066 Å. QMNP's N_2 adsorption-desorption isotherms show Type IV isotherm curves, indicating the existence of mesoporous structures like MNPs and BNPs[89]. Despite having a lesser surface area and pore volume than MNPs and BNPs, QMNPs exhibit mesoporous properties that make them appropriate for a variety of applications.

The TGA profiles for MNPs and BNPs show similar tendencies, with gradual weight decrease, significant alterations at certain temperatures, and a stable plateau. The observed shifts at about 100 °C, 230 °C, 330 °C, and 480 °C for MNPs and 100 °C, 160 °C, 290 °C, and 480 °C for BNPs imply various stages of thermal breakdown or phase transitions within the nanoparticles[90–93]. These changes may be due to the removal of surface-adsorbed water, the decomposition of organic ligands or surfactants, or the oxidation or vaporization of organic moieties or residual solvents. The consistent plateau found beyond these temperature ranges supports the production of stable Zn-based nanoparticles, confirming the materials' thermal stability. The stability of Zn-based nanoparticles at temperatures exceeding 400 °C indicates that they are suitable for high-temperature applications. Similarly, the TGA profile of QMNPs shows a consistent weight decrease with dramatic shifts at certain temperatures, followed by a stable plateau. The shifts seen at 230 °C, 330 °C, and 500 °C represent various stages of thermal breakdown or phase transitions within the nanoparticles[12,94]. The steady plateau beyond these temperature ranges indicates the development of stable nanoparticles, which is consistent with the thermal stability seen for MNPs and BNPs.

5.5. Conclusion

In nanoparticle synthesis, high yield is critical for maximizing nanoparticle production while minimizing waste and resource consumption. Scaling up presents challenges such as maintaining consistent product quality, optimizing reaction conditions for bigger volumes, assuring safety, and minimizing costs. Reactor design, mixing efficiency, heat and mass transmission, safety standards, and environmental considerations are all important factors to consider while scaling up. Before moving into full-scale manufacturing, pilot-scale studies and computational modelling approaches are frequently used to determine scalability and optimize process parameters. Optimization entails progressively increasing the efficiency, productivity, and quality of nanoparticle synthesis processes. Optimization can occur at any stage of the synthesis process, including precursor selection, reaction conditions, purification methods, and post-synthesis manipulation. Electron microscopy, X-ray diffraction, spectroscopy, and thermal analysis are important techniques for determining the internal morphology, crystallinity, chemical composition, thermal stability, and surface properties of these nanoparticles. Such insights are critical in determining their applicability for a wide range of applications, including catalysis, sensing, energy storage, biological diagnostics, and environmental remediation. Because of their asymmetric structure, Janus nanoparticles frequently display anisotropic properties, which means that their qualities change depending on the direction or orientation. Several synthesis strategies, including seed-mediated growth, selective surface modification, template-assisted synthesis, and microfluidic approaches, have been developed to create Janus nanoparticles with fine control over their structure and behaviour.

References

[1] Krishnaraj, C., Ramachandran, R., Mohan, K., and Kalaichelvan, P. T. Optimization for rapid synthesis of silver nanoparticles and its effect on phytopathogenic fungi. *Spectrochimica Acta Part A: Molecular and Biomolecular Spectroscopy*, 93:95-99, 2012.

[2] Langer, K., Balthasar, S., Vogel, V., Dinauer, N., Von Briesen, H., and Schubert, D. Optimization of the preparation process for human serum albumin (HSA) nanoparticles. *International Journal of Pharmaceutics*, 257(1-2):169-180, 2003.

[3] Rodrigues, T. S., Da Silva, A. G. M., and Camargo, P. H. C. Nanocatalysis by noble

metal nanoparticles: controlled synthesis for the optimization and understanding of activities. *Journal of Materials Chemistry A*, 7(11):5857-5874, 2019.

[4] Bessekhouad, Y., Robert, D., and Weber, J. V. Synthesis of photocatalytic TiO2 nanoparticles: optimization of the preparation conditions. *Journal of Photochemistry and Photobiology A: Chemistry*, 157(1):47-53, 2003.

[5] Anulika, N. P., Ignatius, E. O., Raymond, E. S., Osasere, O.-I., and Abiola, A. H. The chemistry of natural product: Plant secondary metabolites. *Int. J. Technol. Enhanc. Emerg. Eng. Res*, 4(8):1-9, 2016.

[6] Hilal, B., Khan, M. M., and Fariduddin, Q. Recent advancements in deciphering the therapeutic properties of plant secondary metabolites: phenolics, terpenes, and alkaloids. *Plant Physiology and Biochemistry*, 211:108674, 2024.

[7] Deshmukh Krishi Vidyapeeth, P., Mangesh Moharil Biotechnology Centre, I. P., Vaibhav Khelurkar Biotechnology Centre, I. C., Ingle, K. P., Deshmukh, A. G., Padole, D. A., Dudhare, M. S., Moharil, M. P., and Khelurkar, V. C. Phytochemicals: Extraction methods, identification and detection of bioactive compounds from plant extracts. *Journal of Pharmacognosy and Phytochemistry*, 6(1):32-36, 2017. https://www.phytojournal.com/archives/2017.v6.i1.1058/phytochemicals-extraction-methods-identification-and-detection-of-bioactive-compounds-from-plant-extracts. Accessed June 13, 2024.

[8] Leitzmann, C. Characteristics and Health Benefits of Phytochemicals. *Forschende Komplementarmedizin (2006)*, 23(2):69-74, 2016.

[9] Kumar, S. S., Venkateswarlu, P., Rao, V. R., and Rao, G. N. Synthesis, characterization and optical properties of zinc oxide nanoparticles. *International Nano Letters 2013 3:1*, 3(1):1-6, 2013.

[10] Ahmed, S., Annu, Ikram, S., and Yudha, S. Biosynthesis of gold nanoparticles: A green approach. *Journal of Photochemistry and Photobiology B: Biology*, 161:141-153, 2016.

[11] Rather, M. A., Gupta, K., Gupta, A. K., Mishra, P., Qureshi, A., Dutta, T. K., Joardar, S. N., and Mandal, M. *Phytochemical Analysis and Demonstration of Antioxidant, Antibacterial, and Antibiofilm Activities of Ethnomedicinal Plants of North East India*.

Vol 195. Springer US; 2023.

[12] Neto, M. E., Britt, D. W., Jackson, K. A., Almeida Junior, J. H. V., Lima, R. S., Zaia, D. A. M., Inoue, T. T., and Batista, M. A. Synthesis and Characterization of Zinc, Iron, Copper, and Manganese Oxides Nanoparticles for Possible Application as Plant Fertilizers. *Journal of Nanomaterials*, 2023(1):1312288, 2023.

[13] Al-Hada, N. M., Kamari, H. M., Shaari, A. H., and Saion, E. Fabrication and characterization of Manganese–Zinc Ferrite nanoparticles produced utilizing heat treatment technique. *Results in Physics*, 12:1821-1825, 2019.

[14] Quintanar-Guerrero, D., Fessi, H., Allémann, E., and Doelker, E. Influence of stabilizing agents and preparative variables on the formation of poly(d,l-lactic acid) nanoparticles by an emulsification-diffusion technique. *International Journal of Pharmaceutics*, 143(2):133-141, 1996.

[15] Shields, S. P., Richards, V. N., and Buhro, W. E. Nucleation control of size and dispersity in aggregative nanoparticle growth. A study of the coarsening kinetics of thiolate-capped gold nanocrystals. *Chemistry of materials*, 22(10):3212-3225, 2010.

[16] Hu, Y., Lee, B., Bell, C., and Jun, Y. S. Environmentally abundant anions influence the nucleation, growth, ostwald ripening, and aggregation of hydrous Fe(III) oxides. *Langmuir*, 28(20):7737-7746, 2012.

[17] Compton, O. C., and Osterloh, F. E. Evolution of size and shape in the colloidal crystallization of gold nanoparticles. *Journal of the American Chemical Society*, 129(25):7793-7798, 2007.

[18] Das, P., Barua, S., Sarkar, S., Chatterjee, S. K., Mukherjee, S., Goswami, L., Das, S., Bhattacharya, S., Karak, N., and Bhattacharya, S. S. Mechanism of toxicity and transformation of silver nanoparticles: Inclusive assessment in earthworm-microbe-soil-plant system. *Geoderma*, 314:73-84, 2018.

[19] Das, P. T., Goswami, C., and Karmakar, R. M. Utilisation of geospatial technology for characterization, classification and mapping of forest soils of central Brahmaputra valley zone of Assam. *Journal of Pharmacognosy and Phytochemistry*, 10(4):111-118, 2021. https://www.phytojournal.com/archives/2021.v10.i4.14213/utilisation-of-geospatial-technology-for-characterization-classification-and-mapping-of-forest-soils-

of-central-brahmaputra-valley-zone-of-assam. Accessed June 4, 2024.

[20] Barua, S., Konwarh, R., Bhattacharya, S. S., Das, P., Devi, K. S. P., Maiti, T. K., Mandal, M., and Karak, N. Non-hazardous anticancerous and antibacterial colloidal 'green' silver nanoparticles. *Colloids and Surfaces B: Biointerfaces*, 105:37-42, 2013.

[21] Gogoi, N., Babu, P. J., Mahanta, C., and Bora, U. Green synthesis and characterization of silver nanoparticles using alcoholic flower extract of Nyctanthes arbortristis and in vitro investigation of their antibacterial and cytotoxic activities. *Materials Science and Engineering: C*, 46:463-469, 2015.

[22] Almi Putra, R., Andi Fadlly, T., Asmara, V., Monica, D., Sartika, Hijrahnisa, Novia, W., Yakob, M., Indrayana, I., Geubrina Raszky, R., Mujahid Hamdan, A., Arfi, F., Rahwanto, A., and Jalil, Z. The effect of Zn2+ ion substitution on nanoparticles of ZnxMn(1-X) Fe2O4 (X = 0.2, 0.4, 0.6, 0.8) towards signal surface plasmon resonance (SPR). *Materials Research Innovations*, 27(6):420-428, 2023.

[23] Omar, N. A. S., Ramli, I., Fen, Y. W., Abdullah, J., Daud, N. F. M., Daniyal, W. M. E. M. M., and Mahdi, M. A. A sensing approach for manganese ion detection by carbon dots nanocomposite thin film-based surface plasmon resonance sensor. *Optik*, 243:167435, 2021.

[24] Daniel, S., Praveena, M. G., and Mohammed, E. M. Exploration of highly photoluminescent first-row transition metals (manganese, iron, cobalt, nickel, copper and zinc) co-doped nano carbon dots as energy storage materials. *Materials Science and Engineering: B*, 269:115145, 2021.

[25] Raz, S. R., Leontaridou, M., Bremer, M. G. E. G., Peters, R., and Weigel, S. Development of surface plasmon resonance-based sensor for detection of silver nanoparticles in food and the environment. *Analytical and Bioanalytical Chemistry*, 403(10):2843-2850, 2012.

[26] de França Bettencourt, G. M., Degenhardt, J., Zevallos Torres, L. A., de Andrade Tanobe, V. O., and Soccol, C. R. Green biosynthesis of single and bimetallic nanoparticles of iron and manganese using bacterial auxin complex to act as plant bio-fertilizer. *Biocatalysis and Agricultural Biotechnology*, 30:101822, 2020.

[27] Sani, S., Adnan, R., and Mohamed Iqbal, M. A. One-step statistical design of

experiment for the screening and optimization of magnetite nanoparticles yields from solvothermal synthesis. *Microporous and Mesoporous Materials*, 312:110775, 2021.

[28] Hernández-Hernández, A. A., Álvarez-Romero, G. A., Castañeda-Ovando, A., Mendoza-Tolentino, Y., Contreras-López, E., Galán-Vidal, C. A., and Páez-Hernández, M. E. Optimization of microwave-solvothermal synthesis of Fe3O4 nanoparticles. Coating, modification, and characterization. *Materials Chemistry and Physics*, 205:113-119, 2018.

[29] Maleki, © Basir, Siamak, S., Talesh, A., and Maleki, B. Optimization of the Sono-Biodiesel in the Attendance of ZnO Nanoparticles, Process Yield Enhancement: Box Behnken Design. *Journal of Chemical and Petroleum Engineering*, 2022(1):1-14, .

[30] Englebienne, P., Van Hoonacker, A., and Verhas, M. Surface plasmon resonance: principles, methods and applications in biomedical sciences. *Spectroscopy*, 17(2-3):255-273, 2003.

[31] Jana, J., Ganguly, M., and Pal, T. Enlightening surface plasmon resonance effect of metal nanoparticles for practical spectroscopic application. *RSC Advances*, 6(89):86174-86211, 2016.

[32] Wani, I. A., Khatoon, S., Ganguly, A., Ahmed, J., Ganguli, A. K., and Ahmad, T. Silver nanoparticles: Large scale solvothermal synthesis and optical properties. *Materials Research Bulletin*, 45(8):1033-1038, 2010.

[33] Oyetola, E. O. Comparative Studies of Biosynthesized Zinc Oxide Nanoparticles. *Nanochemistry Research*, 8(1):31-39, 2023.

[34] Tsubaki, M., Mogi, T., Anraku, Y., and Hori, H. Structure of the Heme—Copper Binuclear Center of the Cytochrome bo Complex of Escherichia coli: EPR and Fourier Transform Infrared Spectroscopic Studies. *Biochemistry*, 32(23):6065-6072, 1993.

[35] Bellayer, S., Gilman, J. W., Eidelman, N., Bourbigot, S., Flambard, X., Fox, D. M., De Long, H. C., and Trulove, P. C. Preparation of Homogeneously Dispersed Multiwalled Carbon Nanotube/Polystyrene Nanocomposites via Melt Extrusion Using Trialkyl Imidazolium Compatibilizer. *Advanced Functional Materials*, 15(6):910-916, 2005.

[36] Bellayer, S., Gilman, J. W., Eidelman, N., Bourbigot, S., Flambard, X., Fox, D. M., De Long, H. C., and Trulove, P. C. Preparation of homogeneously dispersed trialkyl

imidazolium compatibilized multi walled carbon nanotube/polystyrene nanocomposites via melt extrusion. *Proceedings - Electrochemical Society*, PV 2004-24(1):600-606, 2006.

[37] Yordsri, V., Thanachayanont, C., Asahina, S., Yamaguchi, Y., Kawasaki, M., Oikawa, T., Nobuchi, T., and Shiojiri, M. Scanning Electron Microscopy (SEM) Energy Dispersive X-ray Spectroscopy (EDS) Mapping and In-situ Observation of Carbonization of Culms of Bambusa Multiplex. *Microscopy and Microanalysis*, 24(2):156-162, 2018.

[38] Okano, Y., Nakajima, K., Kikuchi, N., Suga, M., Miyado, T., Kobayashi, T., Matsumoto, T., Sekine, N., Nogami, K., Ikeda, M., Kojima, H., and Nokuo, T. B13-P-02 New High Resolution FE-SEM Capable of High Speed Analysis and Electron-Energy-Selective Imaging. *Microscopy*, 64(suppl_1):i93-i93, 2015.

[39] Wang, R., Liao, S., and Ji, S. High performance Pd-based catalysts for oxidation of formic acid. *Journal of Power Sources*, 180(1):205-208, 2008.

[40] Xue, T., Xu, C. L., Zhao, D. D., Li, X. H., and Li, H. L. Electrodeposition of mesoporous manganese dioxide supercapacitor electrodes through self-assembled triblock copolymer templates. *Journal of Power Sources*, 164(2):953-958, 2007.

[41] Wong, C. C., Li, H. Bin, Cheng, K. W., and Chen, F. A systematic survey of antioxidant activity of 30 Chinese medicinal plants using the ferric reducing antioxidant power assay. *Food Chemistry*, 97(4):705-711, 2006.

[42] Nam, H., Rodriguez-Alejandro, D. A., Adhikari, S., Brodbeck, C., Taylor, S., and Johnson, J. Experimental investigation of hardwood air gasification in a pilot scale bubbling fluidized bed reactor and CFD simulation of jet/grid and pressure conditions. *Energy Conversion and Management*, 168:599-610, 2018.

[43] Darwish, N. N., Shareefdeen, Z. M., El Sayed, Y., Al Zubaidy, I., and Sara, Z. Design and analysis of adsorptive desulphurisation of diesel oil. *International Journal of Oil, Gas and Coal Technology*, 17(3):304-320, 2018.

[44] Pyramides, G., Robinson, J. W., and William Zito, S. The combined use of DSC and TGA for the thermal analysis of atenolol tablets. *Journal of Pharmaceutical and Biomedical Analysis*, 13(2):103-110, 1995.

[45] Prasad, K., and Jha, A. K. ZnO Nanoparticles: Synthesis and Adsorption Study. *Natural Science*, 01(02):129-135, 2009.

[46] Mohd Yusof, H., Abdul Rahman, N. A., Mohamad, R., Zaidan, U. H., and Samsudin, A. A. Optimization of biosynthesis zinc oxide nanoparticles: Desirability-function based response surface methodology, physicochemical characteristics, and its antioxidant properties. *OpenNano*, 8:100106, 2022.

[47] Saha, N., Trivedi, P., and Dutta Gupta, S. Surface Plasmon Resonance (SPR) Based Optimization of Biosynthesis of Silver Nanoparticles from Rhizome Extract of Curculigo orchioides Gaertn. and Its Antioxidant Potential. *Journal of Cluster Science*, 27(6):1893-1912, 2016.

[48] Nath, N., and Chilkoti, A. Label-free biosensing by surface plasmon resonance of nanoparticles on glass: Optimization of nanoparticle size. *Analytical Chemistry*, 76(18):5370-5378, 2004.

[49] Tu, M. H., Sun, T., and Grattan, K. T. V. Optimization of gold-nanoparticle-based optical fibre surface plasmon resonance (SPR)-based sensors. *Sensors and Actuators B: Chemical*, 164(1):43-53, 2012.

[50] Chowdhury, S., Yusof, F., Faruck, M. O., and Sulaiman, N. Process Optimization of Silver Nanoparticle Synthesis Using Response Surface Methodology. *Procedia Engineering*, 148:992-999, 2016.

[51] Lalegani, Z., and Seyyed Ebrahimi, S. A. Optimization of synthesis for shape and size controlled silver nanoparticles using response surface methodology. *Colloids and Surfaces A: Physicochemical and Engineering Aspects*, 595:124647, 2020.

[52] Köhler, M., Goodman Dlamini, N., Kotze Basson, A., and Srirama Rajasekhar Pullabhotla, V. Synthesis and Characterization of Various Bimetallic Nanoparticles and Their Application. *Applied Nano 2023, Vol. 4, Pages 1-24*, 4(1):1-24, 2023.

[53] Dobrescu, G., Papa, F., State, R., Fangli, I., and Balint, I. Particle size distribution of Pt–Cu bimetallic nanoparticles by fractal analysis. *Powder Technology*, 269:532-540, 2015.

[54] Loza, K., Heggen, M., Epple, M., Loza, K., Epple, M., and Heggen, M. Synthesis, Structure, Properties, and Applications of Bimetallic Nanoparticles of Noble Metals.

Advanced Functional Materials, 30(21):1909260, 2020.

[55] Palanikumar, L., Ramasamy, S. N., and Balachandran, C. Size-dependent antimicrobial response of zinc oxide nanoparticles. *IET Nanobiotechnology*, 8(2):111-117, 2014.

[56] Khorsand Zak, A., Razali, R., Abd Majid, W. H., and Darroudi, M. Synthesis and characterization of a narrow size distribution of zinc oxide nanoparticles. *International Journal of Nanomedicine*, 6(1):1399-1403, 2011.

[57] Studart, A. R., Amstad, E., and Gauckler, L. J. Colloidal stabilization of nanoparticles in concentrated suspensions. *Langmuir*, 23(3):1081-1090, 2007.

[58] McKee, C. T., and Walz, J. Y. Interaction forces between colloidal particles in a solution of like-charged, adsorbing nanoparticles. *Journal of Colloid and Interface Science*, 365(1):72-80, 2012.

[59] Weng, X., Guo, M., Luo, F., and Chen, Z. One-step green synthesis of bimetallic Fe/Ni nanoparticles by eucalyptus leaf extract: Biomolecules identification, characterization and catalytic activity. *Chemical Engineering Journal*, 308:904-911, 2017.

[60] Sheny, D. S., Mathew, J., and Philip, D. Phytosynthesis of Au, Ag and Au–Ag bimetallic nanoparticles using aqueous extract and dried leaf of Anacardium occidentale. *Spectrochimica Acta Part A: Molecular and Biomolecular Spectroscopy*, 79(1):254-262, 2011.

[61] Sumbal, Nadeem, A., Naz, S., Ali, J. S., Mannan, A., and Zia, M. Synthesis, characterization and biological activities of monometallic and bimetallic nanoparticles using Mirabilis jalapa leaf extract. *Biotechnology Reports*, 22:e00338, 2019.

[62] Malik, M. A., Albeladi, S. S. R., Al-Maaqar, S. M., Alshehri, A. A., Al-Thabaiti, S. A., Khan, I., and Kamli, M. R. Biosynthesis of Novel Ag-Cu Bimetallic Nanoparticles from Leaf Extract of Salvia officinalis and Their Antibacterial Activity. *Life 2023, Vol. 13, Page 653*, 13(3):653, 2023.

[63] Luo, F., Yang, D., Chen, Z., Megharaj, M., and Naidu, R. Characterization of bimetallic Fe/Pd nanoparticles by grape leaf aqueous extract and identification of active biomolecules involved in the synthesis. *Science of The Total Environment*, 562:526-532, 2016.

[64] Hussein, S., Mahmoud, A. M., Elgebaly, H. A., Hendawy, O. M., Hassanein, E. H. M., Moustafa, S. M. N., Alotaibi, N. F., and Nassar, A. M. Green Synthesis of Trimetallic Nanocomposite (Ru/Ag/Pd)-Np and Its In Vitro Antimicrobial and Anticancer Activities. *Journal of Chemistry*, 2022(1):4593086, 2022.

[65] Kunwar, S., Roy, A., Bhusal, U., Gacem, A., Abdullah, M. M. S., Sharma, P., Yadav, K. K., Rustagi, S., Chatterjee, N., Deshwal, V. K., Park, H. K., and Jeon, B. H. Bio-Fabrication of Cu/Ag/Zn Nanoparticles and Their Antioxidant and Dye Degradation Activities. *Catalysts 2023, Vol. 13, Page 891*, 13(5):891, 2023.

[66] Rao, K. J., and Paria, S. Mixed Phytochemicals Mediated Synthesis of Multifunctional Ag-Au-Pd Nanoparticles for Glucose Oxidation and Antimicrobial Applications. *ACS Applied Materials and Interfaces*, 7(25):14018-14025, 2015.

[67] Alshehri, A. A., and Malik, M. A. Facile One-Pot Biogenic Synthesis of Cu-Co-Ni Trimetallic Nanoparticles for Enhanced Photocatalytic Dye Degradation. *Catalysts 2020, Vol. 10, Page 1138*, 10(10):1138, 2020.

[68] Vaseghi, Z., Tavakoli, O., and Nematollahzadeh, A. Rapid biosynthesis of novel Cu/Cr/Ni trimetallic oxide nanoparticles with antimicrobial activity. *Journal of Environmental Chemical Engineering*, 6(2):1898-1911, 2018.

[69] Nam, K. M., Kim, Y. Il, Jo, Y., Lee, S. M., Kim, B. G., Choi, R., Choi, S. Il, Song, H., and Park, J. T. New crystal structure: Synthesis and characterization of hexagonal wurtzite MnO. *Journal of the American Chemical Society*, 134(20):8392-8395, 2012.

[70] Xu, Y. N., and Ching, W. Y. Calculation of ground-state and optical properties of boron nitrides in the hexagonal, cubic, and wurtzite structures. *Physical Review B*, 44(15):7787, 1991.

[71] Anna Fontcuberta Morral, B., Arbiol, J., Daniel Prades, J., Cirera, A., and Ramon Morante, J. Synthesis of Silicon Nanowires with Wurtzite Crystalline Structure by Using Standard Chemical Vapor Deposition**. 20072007.

[72] Tang, Z., Chen, Y., and Ye, W. Calculation of Surface Properties of Cubic and Hexagonal Crystals through Molecular Statics Simulations. *Crystals 2020, Vol. 10, Page 329*, 10(4):329, 2020.

[73] Sarney, W. L. *Hexagonal Close-Packed (Hcp) Crystallography, Diffraction, and*

Indexing Conventions. Tech. rep; 2020.

[74] Wu, C. C., Chung, P. W., Aubry, S., Munday, L. B., and Arsenlis, A. The strength of binary junctions in hexagonal close-packed crystals. *Acta Materialia*, 61(9):3422-3431, 2013.

[75] Pudukudy, M., and Yaakob, Z. Facile Synthesis of Quasi Spherical ZnO Nanoparticles with Excellent Photocatalytic Activity. *Journal of Cluster Science*, 26(4):1187-1201, 2015.

[76] Albu-Yaron, A., Levy, M., Tenne, R., Popovitz-Biro, R., Weidenbach, M., Bar-Sadan, M., Houben, L., Enyashin, A. N., Seifert, G., Feuermann, D., Katz, E. A., and Gordon, J. M. Inorganic Fullerenes MoS 2 Hybrid Nanostructures: From Octahedral to Quasi-Spherical Shells within Individual Nanoparticles**.

[77] Jing, H., and Wang, H. Structural evolution of Ag-Pd bimetallic nanoparticles through controlled galvanic replacement: Effects of mild reducing agents. *Chemistry of Materials*, 27(6):2172-2180, 2015.

[78] Lu, P. J., Huang, S. C., Chen, Y. P., Chiueh, L. C., and Shih, D. Y. C. Analysis of titanium dioxide and zinc oxide nanoparticles in cosmetics. *Journal of Food and Drug Analysis*, 23(3):587-594, 2015.

[79] Snedeker, L. P., Risbud, A. S., Masala, O., Zhang, J. P., and Seshadri, R. Organic phase conversion of bulk (wurtzite) ZnO to nanophase (wurtzite and zinc blende) ZnO. *Solid State Sciences*, 7(12):1500-1505, 2005.

[80] Díaz-Reyes, J., Castillo-Ojeda, R. S., Sánchez-Espíndola, R., Galván-Arellano, M., and Zaca-Morán, O. Structural and optical characterization of wurtzite type ZnS. *Current Applied Physics*, 15(2):103-109, 2015.

[81] Freire-Fernández, F., Reese, T., Rhee, D., Guan, J., Li, R., Schaller, R. D., Schatz, G. C., and Odom, T. W. Quasi-Random Multimetallic Nanoparticle Arrays. *ACS Nano*, 17(21):21905-21911, 2023.

[82] Thongtem, T., Phuruangrat, A., and Thongtem, S. Characterization of nanostructured ZnO produced by microwave irradiation. *Ceramics International*, 36(1):257-262, 2010.

[83] Moreau, J. W., Webb, R. I., and Banfield, J. F. Ultrastructure, aggregation-state, and

crystal growth of biogenic nanocrystalline sphalerite and wurtzite. *American Mineralogist*, 89(7):950-960, 2004.

[84] Verrier, C., Appert, E., Chaix-Pluchery, O., Rapenne, L., Rafhay, Q., Kaminski-Cachopo, A., and Consonni, V. Effects of the pH on the Formation and Doping Mechanisms of ZnO Nanowires Using Aluminum Nitrate and Ammonia. *Inorganic Chemistry*, 56(21):13111-13122, 2017.

[85] Junliang, L., Wei, Z., Cuijing, G., and Yanwei, Z. Synthesis and magnetic properties of quasi-single domain M-type barium hexaferrite powders via sol–gel auto-combustion: Effects of pH and the ratio of citric acid to metal ions (CA/M). *Journal of Alloys and Compounds*, 479(1-2):863-869, 2009.

[86] Zhang, G. Y., Sun, Y. Q., Gao, D. Z., and Xu, Y. Y. Quasi-cube ZnFe2O4 nanocrystals: Hydrothermal synthesis and photocatalytic activity with TiO2 (Degussa P25) as nanocomposite. *Materials Research Bulletin*, 45(7):755-760, 2010.

[87] Bin, D., Guo, Z., Tamirat, A. G., Ma, Y., Wang, Y., and Xia, Y. Crab-shell induced synthesis of ordered macroporous carbon nanofiber arrays coupled with MnCo2O4 nanoparticles as bifunctional oxygen catalysts for rechargeable Zn–air batteries. *Nanoscale*, 9(31):11148-11157, 2017.

[88] Chauhan, N., Singh, V., Kumar, S., Kumari, M., and Sirohi, K. Preparation of silver and nitrogen co-doped mesoporous zinc oxide nanoparticles by evaporation induced self assembly process to study their photocatalytic activity. *Journal of Sol-Gel Science and Technology*, 90(2):390-403, 2019.

[89] Katoch, V., Singh, J., Raj, N., Ravinder, S. &, Singh, P., Sharma, N. R., and Singh, R. P. Synthesis and characterization of mesoporous zinc oxide nanoparticles. *Inorganic and Nano-Metal Chemistry*, October 20212021.

[90] Wang, L., and Muhammed, M. Synthesis of zinc oxide nanoparticles with controlled morphology. *Journal of Materials Chemistry*, 9(11):2871-2878, 1999.

[91] Menazea, A. A., Ismail, A. M., and Samy, A. Novel Green Synthesis of Zinc Oxide Nanoparticles Using Orange Waste and Its Thermal and Antibacterial Activity. *Journal of Inorganic and Organometallic Polymers and Materials*, 31(11):4250-4259, 2021.

[92] Charde, S. J., Sonawane, S. S., Rathod, A. P., Sonawane, S. H., Shimpi, N. G., and Parate, V. R. Copper-doped zinc oxide nanoparticles: Influence on thermal, thermo mechanical, and tribological properties of polycarbonate. *Polymer Composites*, 39(S3):E1398-E1406, 2018.

[93] Sajjad, M., Ullah, I., Khan, M. I., Khan, J., Khan, M. Y., and Qureshi, M. T. Structural and optical properties of pure and copper doped zinc oxide nanoparticles. *Results in Physics*, 9:1301-1309, 2018.

[94] Lachowicz, D., Stroud, J., Hankiewicz, J. H., Gassen, R., Kmita, A., Stepień, J., Celinski, Z., Sikora, M., Zukrowski, J., Gajewska, M., and Przybylski, M. One-Step Preparation of Highly Stable Copper-Zinc Ferrite Nanoparticles in Water Suitable for MRI Thermometry. *Chemistry of Materials*, 34(9):4001-4018, 2022.